Prestack Gaussian-beam depth migration

N. Ross Hill*

ABSTRACT

Kirchhoff migration is the most popular method of three-dimensional prestack depth migration because of its flexibility and efficiency. Its effectiveness can become limited, however, when complex velocity structure causes multipathing of seismic energy. An alternative is Gaussian beam migration, which is an extension of Kirchhoff migration that overcomes many of the problems caused by multipathing. Unlike first-arrival and most-energetic-arrival methods, which retain only one traveltime, this alternative method retains most arrivals by the superposition of Gaussian beams.

This paper presents a prestack Gaussian beam migration method that operates on common-offset gathers. The method is efficient because the computation of beam superposition isolates summations that do not depend on the seismic data and evaluates these integrals by considering their saddle points. Gaussian beam migration of the two-dimensional Marmousi test data set demonstrates the method's effectiveness for structural imaging in a case where there is multipathing of seismic energy.

INTRODUCTION

The purpose of depth migration is to form subsurface images where rapid lateral variations in the earth's velocities cause significant refraction of seismic energy. Problems that require depth migration are imaging beneath salt masses, near fault shadows, and in thrust belts. Since the earth's velocity variations most often can be realistically represented only in three dimensions, the depth migration program should operate efficiently in three dimensions. Also, the depth migration often must be prestack because the assumptions of poststack processing—that a stack is the same as a zero-offset section and that the subsurface is adequately illuminated at zero offset—break down when there are rapid velocity variations. Imaging that requires depth migration often requires it to be both three-dimensional and prestack.

Accurate depth migrations could best be achieved by full-waveform methods, such as finite-difference migration, because these methods best extrapolate the wavefield where there are rapidly varying seismic velocities. Unfortunately, full-waveform migration is not currently practical for prestack migration of most three-dimensional surveys. Efficient full-waveform migration favors recorded wavefields that are the results of single physical experiments, specifically shot or receiver gathers. Standard three-dimensional surveys do not provide dense, areal sampling of these gathers.

Currently, the Kirchhoff method is the almost universal choice for prestack three-dimensional depth migration because it operates efficiently for standard recording geometries. The principal limitations of the Kirchhoff method are caused by the high-frequency wavefield assumptions (Nichols, 1996; Audebert et al., 1997), which are usually invoked to construct the Green's functions for the Kirchhoff summations. In particular, the frequency ω is considered to be large and the approximation

$$G(\mathbf{r}, \mathbf{r}'; \omega) \approx A(\mathbf{r}, \mathbf{r}') \exp[i\omega T(\mathbf{r}, \mathbf{r}')] \qquad (1)$$

is assumed to be an adequate representation of the response at point $\mathbf{r}$ to a point source at $\mathbf{r}'$. Traveltime $T(\mathbf{r}, \mathbf{r}')$ and amplitude $A(\mathbf{r}, \mathbf{r}')$ are frequency-independent solutions to the eikonal and transport equations. Undoubtedly, approximation (1) is inadequate for descriptions of some exploration seismic reflection data, and the assumptions of high frequency that lead to expression (1) must be abandoned. A more usual difficulty, however, is not that these assumptions are hopelessly invalid, but that $T(\mathbf{r}, \mathbf{r}')$ is a multivalued function because of multipathing of the seismic energy. In that case, the single term on the right-hand side of expression (1) should be replaced by a sum of such terms for all the different arrivals.

Retaining all the arrivals is difficult to achieve in a practical three-dimensional depth migration program. When there is complex velocity structure, subsurface points may have no raypath arrivals, one, or many. Not only must a table of traveltimes contain multiple entries at each spatial point, but it must also contain information to ensure that interpolations are between points on the same branch of the traveltime function.

Even if these difficulties with the traveltime function $T(\mathbf{r}, \mathbf{r}')$ are overcome, there remains the problem that the amplitude function $A(\mathbf{r}, \mathbf{r}')$ will be rapidly varying and unbounded when the traveltimes are multivalued.

Figure 1 is an example of multipathing. A low-velocity zone refracts the energy, causing the wavefront to triplicate. The usual approach to dealing with multivalued traveltimes is either to choose the first arrival or to choose the most energetic arrival. The advantage of first arrivals is that they can be efficiently computed by directly solving the eikonal equation. In many cases, first arrivals provide an adequate image. The disadvantage of only retaining the first arrivals is that this method omits the trailing segments of the wavefront where, in fact, the wavefield has the largest amplitudes. In this case, the most energetic arrival may provide a much better image although, in general, the most energetic arrivals might not contain all the important structural information for the image. Moreover, the loci of the most energetic arrivals jump discontinuously from the leading branch of the wavefront back to the high-amplitude cusps (Nichols, 1996). The discontinuities in the most-energetic-arrival times might degrade the performance of the Kirchhoff migration because the key operation of Kirchhoff migration is constructive superposi-

tion along the envelopes of many traveltime curves (Bleistein, 1999).

Gaussian beam migration is an alternative method of prestack Kirchhoff depth migration. This method includes image contributions from most multipath arrivals. The Green's functions are formed by superimposing Gaussian beams to form point-source wavefields. For example, superposition of the beams formed about all the raypaths in Figure 1 can represent the point source and retain the triplication in the wavefield. To the extent that the beams are accurate solutions to the wave equation, this superposition gives the correct point-source response in regions where the velocities vary and the wavefront triplicates. This Gaussian beam summation technique can be developed as an efficient, three-dimensional, prestack, common-offset depth migration.

THEORY

Just as other migration methods, Gaussian beam migration begins with the assumption that the scalar wave equation governs a seismic wavefield $\phi(\mathbf{r}, \omega)$:

$$\nabla^2\phi(\mathbf{r}, \omega) + \frac{\omega^2}{v^2(\mathbf{r})}\phi(\mathbf{r},\omega) = 0, \tag{2}$$

where $v(\mathbf{r})$ is the seismic velocity at point $\mathbf{r}$. Values of this wavefield are related by boundary value integrals. In particular, the upcoming wavefield recorded at the earth's surface $z' = 0$ is related to the field at a subsurface point $\mathbf{r}$ by the boundary value integral

$$\phi(\mathbf{r}, \omega) = \frac{-1}{2\pi} \iint dx'\, dy' \frac{\partial G^*(\mathbf{r}, \mathbf{r}', \omega)}{\partial z'}\phi(\mathbf{r}', \omega), \tag{3}$$

where $\mathbf{r}' = (x', y', 0)$ are the detector positions at the earth's surface $z' = 0$. A Green's function $G(\mathbf{r}, \mathbf{r}', \omega)$ is the response at point $\mathbf{r}$ to a source at point $\mathbf{r}'$, and obeys equation (2) with the right-hand side replaced by the delta function $-4\pi\delta(\mathbf{r}-\mathbf{r}')$. There are two independent Green's function solutions corresponding to different radiation boundary conditions: if $G(\mathbf{r}, \mathbf{r}', \omega)$ is the retarded solution, which represents the waves expanding from the point source, then its complex conjugate $G^*(\mathbf{r}, \mathbf{r}', \omega)$ is the advanced solution, which represents waves imploding toward the point source. Function $G^*(\mathbf{r}, \mathbf{r}', \omega)$ is the appropriate choice in the present case, which requires that the recorded wavefield be propagated back toward the subsurface reflectors (Schneider, 1978).

Gaussian beams enter the current derivation by expressing the Green's function as a Gaussian-beam summation. Appendix B shows that a high-frequency representation of the field at point $\mathbf{r}$ caused by source at point $\mathbf{r}'$ is

$$G(\mathbf{r}, \mathbf{r}'; \omega) \approx \frac{i\omega}{2\pi} \iint \frac{dp_x'\, dp_y'}{p_z'}\, u_{GB}(\mathbf{r}; \mathbf{r}', \mathbf{p}'; \omega), \tag{4}$$

where $u_{GB}(\mathbf{r}; \mathbf{r}', \mathbf{p}'; \omega)$ is the normalized beam (A-9) with initial conditions (A-10) and (A-11). The raypath for beam $u_{GB}(\mathbf{r}; \mathbf{r}', \mathbf{p}'; \omega)$ radiates from point $\mathbf{r}'$ with ray vector $\mathbf{p}'$.

Green's function (4) requires that the source point coincides with the initial point of the rays. Since seismic reflection surveys have closely spaced sources and detectors, however, equation (4) should be modified so that the source point $\mathbf{r}'$ can be different from the initial point of the rays $\mathbf{r}_0$. A simple way to do this modification is to insert a factor in the integrand of
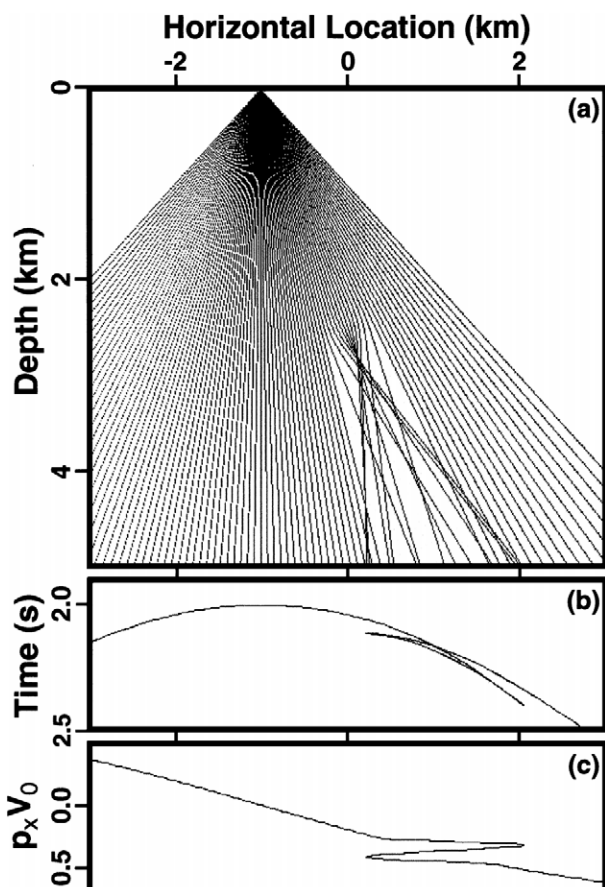

FIG. 1. A low-velocity zone causes crossing rays (a). Multipathing of rays with initial directions p_x (c) cause the triplication of the traveltimes (b) at depth $z = 5000$ m. The background velocity is constant 2500 m/s. The low-velocity zone is a cosine-tapered spherical inclusion of radius 300 m and magnitude -500 m/s centered at $x = 0$, $z = 2500$ m.

equation (4) to compensate for the phase change from points $\mathbf{r}_0$ to $\mathbf{r}'$:

$$G(\mathbf{r}, \mathbf{r}'; \omega) \approx \frac{i\omega}{2\pi} \iint \frac{dp'_x dp'_y}{p'_z} u_{GB}(\mathbf{r}; \mathbf{r}_0, \mathbf{p}'; \omega)$$
$$\cdot \exp[-i\omega\, \mathbf{p}' \cdot (\mathbf{r}' - \mathbf{r}_0)]. \tag{5}$$

Equation (5) is valid for source points $\mathbf{r}'$ in some neighborhood of the ray initial point $\mathbf{r}_0$. Since an additional phase factor has been introduced into the integrand, the saddle-point integration in Appendix B should also include it. These modifications, however, do not result in large corrections and make little difference in migrated images. This derivation proceeds by using the simple approximation (5).

To use Green's function (5) in the Kirchhoff summation (3), the range of integration in equation (3) must be partitioned into small regions. Within each region, a different raypath initial point $\mathbf{r}_0$ can be used in the Green's function (5) to ensure that the boundary point $\mathbf{r}'$ is always near $\mathbf{r}_0$. This partitioning is accomplished by inserting into the integrand of equation (3) overlapping Gaussian functions that sum approximately to unity for any x and y:

$$\frac{\sqrt{3}}{4\pi} \left| \frac{\omega}{\omega_\ell} \right| \left(\frac{a}{w_\ell} \right)^2 \sum_{\mathbf{L}} \exp\left[-\left| \frac{\omega}{\omega_\ell} \right| \frac{|\mathbf{r}' - \mathbf{L}|^2}{2w_\ell^2} \right] \approx 1. \tag{6}$$

Vector $\mathbf{L} = (L_x, L_y, 0)$ ranges over a two-dimensional lattice of points that spans the range of the recorded seismic data. The Gaussian width w_ℓ is the same as the initial beam width (see Appendix A). Constant a is the distance between nearest-neighbor lattice points. The normalization factor in equation (6) is appropriate for a hexagonal lattice, which optimizes the approximation.

Boundary value integral (3), Green's function (5), and the partitioning function (6) are all that are necessary to develop both poststack and prestack Gaussian beam migration. The first step is to develop the poststack formulation and then to extend this formulation to a prestack method, which operates on common-offset data in a way that is similar to the poststack migration.

Poststack image

The exploding reflector principle (Claerbout, 1985) states that if the seismic velocities are halved, then the seismic image is equal to the downward-continued, zero-offset data evaluated at time zero. If $\phi_0(\mathbf{r}, t)$ is the zero-offset wavefield at subsurface point $\mathbf{r}$, then the image is

$$I_0(\mathbf{r}) = [\phi_0(\mathbf{r}, t)]_{t=0} = \int d\omega\, \phi_0(\mathbf{r}, \omega). \tag{7}$$

Since the wavefield at subsurface points is determined by the boundary integral (3), equation (7) becomes

$$I_0(\mathbf{r}) = \frac{-1}{2\pi} \int d\omega \iint dx'\, dy' \frac{\partial G^*(\mathbf{r}, \mathbf{r}'; \omega)}{\partial z'} [D_{\mathbf{h}}(\mathbf{r}', \omega)]_{\mathbf{h}=0}, \tag{8}$$

where $D_{\mathbf{h}}(\mathbf{r}')$ is the recorded wavefield at offset $\mathbf{h}$. If equation (6) is inserted into the integrand of equation (8) and the Green's function is represented by function (5) with $\mathbf{r}_0 = \mathbf{L}$, equation (8) becomes

$$I_0(\mathbf{r}) \approx -C_0 \sum_{\mathbf{L}} \int d\omega \iint dp'_x\, dp'_y\, u^*_{GB}(\mathbf{r}; \mathbf{L}, \mathbf{p}'; \omega)$$
$$\times [D_{\mathbf{h}}(\mathbf{L}, \mathbf{p}', \omega)]_{\mathbf{h}=0}, \tag{9}$$

where C_0 is the constant

$$C_0 = \frac{\sqrt{3}}{4\pi} \left(\frac{\omega_\ell a}{w_\ell} \right)^2. \tag{10}$$

The function $D_{\mathbf{h}}(\mathbf{L}, \mathbf{p}, \omega)$ is the transformed data

$$D_{\mathbf{h}}(\mathbf{L}, \mathbf{p}', \omega) = \left| \frac{\omega}{\omega_\ell} \right|^3 \iint \frac{dx'dy'}{4\pi^2} D_{\mathbf{h}}(\mathbf{r}', \omega)$$
$$\times \exp\left[i\omega\mathbf{p}' \cdot (\mathbf{r}' - \mathbf{L}) - \left| \frac{\omega}{\omega_\ell} \right| \frac{|\mathbf{r}' - \mathbf{L}|^2}{2w_\ell^2} \right]. \tag{11}$$

Transformation (11) is a local slant stack of the common-offset traces. This transformation separates the data into beam components. Each beam component contains the recorded energy that is partially localized in space about midpoint $\mathbf{L}$ and partially localized in dip about vector $\mathbf{p}'$. This transformation does not depend on the velocity model, although the range of vector $\mathbf{p}'$ does depend on the velocities at the earth's surface.

Equations (9) and (11) are a simple formulation of poststack migration, which has been previously derived by another, more detailed approach (Hill, 1990). As in the previous approach, the energy recorded in a zero-offset gather is separated into components according to location and dip [transformation (11)], and each of these components is projected back into the earth along a Gaussian beam and added to the image [summation (9)].

Prestack image

Gaussian beam migration can be extended to prestack migration by using the updown imaging principle (Claerbout, 1970, 1976). This principle states that the image is formed by crosscorrelating the downward-continued, recorded wavefield and the forward-modeled source wavefield. This imaging principle is kinematically correct but results in image amplitudes that depend upon illumination strength, rather than only on the earth's reflection coefficients (Claerbout, 1976). In the Fourier domain, this crosscorrelation of the two wavefields corresponds to summing over frequency the product of the downward-continued wavefield and the complex conjugate of the source wavefield. The boundary-value integral (3) provides the downward-continued recorded wavefield, and $G(\mathbf{r}, \mathbf{r}_s; \omega)$ is the wavefield radiating from a source at position $\mathbf{r}_s$. Summing contributions from all sources results in the image

$$I(\mathbf{r}) = \frac{-1}{2\pi} \int d\omega \iint dx_d\, dy_d \iint dx_s dy_s \frac{\partial G^*(\mathbf{r}, \mathbf{r}_d; \omega)}{\partial z_d}$$
$$\times G^*(\mathbf{r}, \mathbf{r}_s; \omega) D(\mathbf{r}_d, \mathbf{r}_s, \omega). \tag{12}$$

Function $D(\mathbf{r}_d, \mathbf{r}_s, \omega)$ is the field recorded by a detector at point $\mathbf{r}_d = (x_d, y_d, 0)$ when the source is located at $\mathbf{r}_s = (x_s, y_s, 0)$.

Instead of summing directly over source and receiver positions, as in equation (12), the present formulation emphasizes the application of the imaging operation to common-offset gathers. Accordingly, the integration variables are changed to midpoint $\mathbf{r}_m$ and offset $\mathbf{h}$ coordinates:

$$\mathbf{r}_m = \tfrac{1}{2}(\mathbf{r}_d + \mathbf{r}_s),$$
$$\mathbf{h} = \tfrac{1}{2}(\mathbf{r}_d - \mathbf{r}_s). \tag{13}$$

Equation (12) becomes

$$I(\mathbf{r}) = \iint dh_x \, dh_y \, I_\mathbf{h}(\mathbf{r}) \tag{14}$$

$$I_\mathbf{h}(\mathbf{r}) = \frac{-2}{\pi} \int d\omega \iint dx_m \, dy_m \, D_\mathbf{h}(\mathbf{r}_m, \omega)$$
$$\times \frac{\partial G^*(\mathbf{r}, \mathbf{r}_d; \omega)}{\partial z_d} G^*(\mathbf{r}, \mathbf{r}_s; \omega), \tag{15}$$

where $D_\mathbf{h}(\mathbf{r}_m, \omega)$ is the field recorded at midpoint $\mathbf{r}_m$ and offset $\mathbf{h}$. The summation (15) is the seismic image from data collected at the common-offset specified by the offset vector $\mathbf{h}$. The integral (14) sums the results of common-offset migrations (15) into a final image.

To use the Green's function representation (5) in integral (15), the integrand must be partitioned into regions by equation (6). Within each region, the ray origins for $G(\mathbf{r}, \mathbf{r}_d; \omega)$ and $G(\mathbf{r}, \mathbf{r}_s; \omega)$ are chosen to be at $\mathbf{r}_0 = \mathbf{L} + \mathbf{h}$ and $\mathbf{r}_0 = \mathbf{L} - \mathbf{h}$ (see Figure 2b). These steps result in

$$I_\mathbf{h}(\mathbf{r}) \approx \frac{2i\omega}{\pi} C_0 \sum_\mathbf{L} \int d\omega \iint dp_x^d \, dp_y^d$$
$$\times \iint \frac{dp_x^s \, dp_y^s}{p_z^s} u_{GB}^*(\mathbf{r}; \mathbf{L} + \mathbf{h}, \mathbf{p}^d; \omega)$$
$$\times u_{GB}^*(\mathbf{r}; \mathbf{L} - \mathbf{h}, \mathbf{p}^s; \omega) D_\mathbf{h}(\mathbf{L}, \mathbf{p}^d + \mathbf{p}^s, \omega). \tag{16}$$

Equation (16) becomes more manageable if the integration variables are changed to new variables $\mathbf{p}^m = (p_x^m, p_y^m)$ and $\mathbf{p}^h = (p_x^h, p_y^h)$, such that

$$p_x^m = p_x^d + p_x^s,$$
$$p_y^m = p_y^d + p_y^s,$$
$$p_x^h = p_x^d - p_x^s,$$
$$p_y^h = p_y^d - p_y^s. \tag{17}$$

The new variables correspond to the time dip in common offset and common midpoint gathers. With these variable changes, equation (16) becomes

$$I_\mathbf{h}(\mathbf{r}) \approx -C_0 \sum_\mathbf{L} \int d\omega \iint dp_x^m \, dp_y^m \, U_\mathbf{h}(\mathbf{r}; \mathbf{L}, \mathbf{p}^m; \omega)$$
$$\times D_\mathbf{h}(\mathbf{L}, \mathbf{p}^m, \omega), \tag{18}$$

where $D_\mathbf{h}(\mathbf{L}, \mathbf{p}^m, \omega)$ is the transformation (11) for data of offset $\mathbf{h}$ and

$$U_\mathbf{h}(\mathbf{r}; \mathbf{L}, \mathbf{p}^m; \omega) = \frac{-i\omega}{2\pi} \iint \frac{dp_x^h \, dp_y^h}{p_z^s} u_{GB}^*(\mathbf{r}; \mathbf{L} + \mathbf{h}, \mathbf{p}^d; \omega)$$
$$\times u_{GB}^*(\mathbf{r}; \mathbf{L} - \mathbf{h}, \mathbf{p}^s; \omega) \tag{19}$$

describes the propagation of wavefield component $D_\mathbf{h}(\mathbf{L}, \mathbf{p}^m, \omega)$. The sum and difference of the two-dimensional vectors $\mathbf{p}^m$ and $\mathbf{p}^h$ determine the initial directions $\mathbf{p}^d$ and $\mathbf{p}^s$ of the beams in the integrand of equation (19).

Equation (18) is similar to the poststack summation (9). Just as for the poststack case, transformation (11) separates the recorded energy according to its location and dip on a common offset gather, although in this case the offset can be finite. In this prestack case, the description of the component's propagation is more complicated than in the poststack case. The propagation described by equation (19) includes all pairs of raypaths from the source and detector such that their dips are in accord with equation (17). As depicted in Figure 2, the dips of the shot ray and the receiver ray must sum to $\mathbf{p}^m$, which is equal to the dip of the data component $D_\mathbf{h}(\mathbf{L}, \mathbf{p}^m, \omega)$.

Efficient evaluation of summation (19) is key to prestack Gaussian beam migration. This summation over the product of source and detector beams does not depend on the recorded data, suggesting that traveltime description is the essential role of equation (19). Large contributions to the summation occur if both the beams pass near the point $\mathbf{r}$ for the same value of $\mathbf{p}^h$ (see Figure 2). In general, the raypaths of both beams will not pass through $\mathbf{r}$ at the same value of $\mathbf{p}^h$. Contributions to the summation (19) could be evaluated by the method of steepest
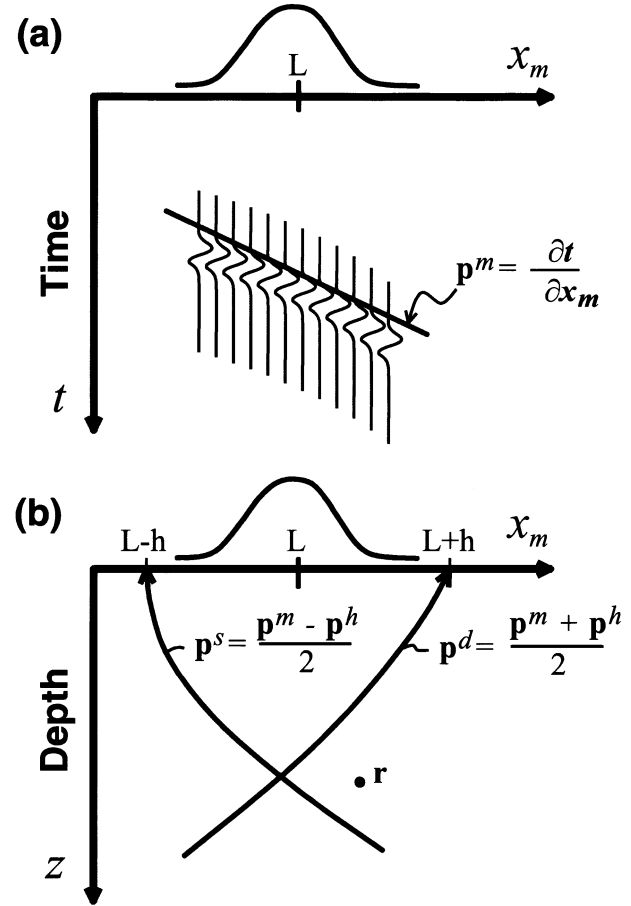

FIG. 2. (a) The beam steering transform [Equation (11)] separates events near location L having dip $\mathbf{p}^m$. (b) These events are projected back into the earth along all shot-detector raypath pairs that have dips summing to $\mathbf{p}^m$.

descents (Aki and Richards, 1980). Expression (19) may be written as

$$U_{\mathbf{h}}(\mathbf{r}; \mathbf{L}, \mathbf{p}^m; \omega) = \frac{-i\omega}{2\pi} \iint \frac{dp_x^h dp_y^h}{p_z^s} A(\mathbf{r}; \mathbf{p}^m, \mathbf{p}^h)$$
$$\times \exp[i\omega T(\mathbf{r}; \mathbf{p}^m, \mathbf{p}^h)] \qquad (20)$$

by using equation (A-9). Function $A(\mathbf{r}; \mathbf{p}^m, \mathbf{p}^h)$ is the product of amplitudes of the two beams; $T(\mathbf{r}; \mathbf{p}^m, \mathbf{p}^h)$ is the sum of the complex traveltimes

$$T(\mathbf{r}; \mathbf{p}^m, \mathbf{p}^h) = T_d(\mathbf{r}; \mathbf{p}^d) + T_s(\mathbf{r}; \mathbf{p}^s), \qquad (21)$$

where $T_d(\mathbf{r}; \mathbf{p}^d)$ and $T_s(\mathbf{r}; \mathbf{p}^s)$ are the complex traveltimes for the beams coming from detector and source points $\mathbf{r}_d$ and $\mathbf{r}_s$ with initial ray vectors $\mathbf{p}^d$ and $\mathbf{p}^s$. Steepest-descents evaluation would result in

$$U_{\mathbf{h}}(\mathbf{r}; \mathbf{L}, \mathbf{p}^m; \omega) \approx A_0 \exp[i\omega T_0], \qquad (22)$$

where T_0 is the complex traveltime (21) evaluated at the saddle point and A_0 is a complex amplitude. The amplitude A_0 does not depend on frequency because the steepest-descents evaluation of the two-dimensional integral generates a factor ω^{-1} that cancels the factor ω appearing in equation (20). A steepest-descents evaluation of (20) would determine A_0 from a second-order expansion of $T(\mathbf{r}; \mathbf{p}^m, \mathbf{p}^h)$ about its saddle points. This expansion could be achieved by using the same dynamic-ray-tracing information used to construct the Gaussian beams. This added effort to determine A_0 is unwarranted in the present theory, however, because the imaging principle used is only kinematically correct.

The present goal of Gaussian beam migration is to form structurally correct images; the image amplitudes are secondary. For this limited goal, the following method provides a simple, fast evaluation of equation (19). The first step is to assume that equation (19) can be reduced to the form (22), which is tantamount to assuming the integral is dominated by contributions near an isolated saddle point. To further simplify the evaluation of equation (19), the second step is to assume that the saddle point of $T(\mathbf{r}; \mathbf{p}^m, \mathbf{p}^h)$ occurs at real $\mathbf{p}^h$. In that case, the saddle point can be located by scanning all real values of $\mathbf{p}^h$ for the value that minimizes the imaginary part of $T(\mathbf{r}; \mathbf{p}^m, \mathbf{p}^h)$. The last step is to use the geometric average of the amplitude of the two beams for the value of A_0. An advantage of this A_0 is that the prestack and poststack migrations will give similar results when applied to a zero-offset gather.

Of course, the complex time (21) will not always have the isolated saddle points that are supposed by the approximation (22). In fact, just as for Green's function approximation (1), approximation (22) will not be valid in some cases where there are multivalued traveltimes. Nevertheless, since equation (17) restricts the domain of the traveltimes included in equation (20), it also restricts multipath contributions to this integral, although it does not eliminate these contributions. For example, Figures 1–4 depict a case in which a low-velocity zone causes triplication of the traveltimes. For this two-dimensional example, the source field in summation (19) is represented by Gaussian beams radiating from the source position $x_s = -1000$ m, and the detector field is represent by beams radiating from position $x_d = 1000$ m (i.e., L = 0, h = 1000 m). Figure 1a shows the raypaths from the source position $x_s = -1000$ m. Because the velocity model is symmetric

about the line $x = 0$, the same rays mirrored about this line would show the rays from the detector position $x_d = 1000$ m. Figure 3 maps the amplitudes of the integrand of (19) as a function of p_x^d and p_x^s for three subsurface points that are affected by the triplication in traveltimes. For integral (19), the summation occurs along a path $p_x^d + p_x^s = p_x^m$ for a given value of p_x^m. The diagonal lines in Figure 3 indicate such paths. If there is a single, dominant peak in the integrand's amplitude along the diagonal path, then the approximation (22) will be a good one.

In most cases, the above method of evaluating equation (19) will retain multipath arrivals. For example, Figure 3c shows a case in which there are two regions of the (p_x^d, P_x^s) plane that cause strong contributions to the image. Two different arrivals from the shotpoint cause the two regions: a first arrival, which has not been affected by the low velocity zone, and a later one, which has been strongly refracted. Contributions to the image from the first arrival occur when integral (19) is evaluated along the path $V_0 \cdot p_x^m = 0.72$. Figure 4e shows the real and imaginary parts of the traveltime for this path. The minimum value of the imaginary part of the traveltime occurs at $V_0 \cdot p_x^h = -0.32$, at which point the value of the complex traveltime is (4.372, 0.0). This is the value of T_0 that is used in approximation (22). The other contributions to equation (19) caused by the later arrival, occurring near $V_0 \cdot p_x^h = 0.02$, are negligible because the imaginary part of the traveltime is always large along this part of the path. The image contribution from the later arrival is included when equation (19) is evaluated at $V_0 \cdot p_x^m = 0.53$. In this case, the minimum value of the imaginary part of T occurs at $V_0 \cdot p_x^h = -0.13$, where the traveltime is (4.431, 0.0) (Figure 4f). Along this path, contributions from the first arrival are negligible.

There is an advantage of searching for the minimum imaginary part of the traveltime instead of the maximum real part. Although these two points will coincide at a saddle point, using the minimum imaginary part tends to select the most significant saddle point, when there are contributions from more than one. For example, in Figure 4e, the global maximum of the real traveltime occurs at $V_0 \cdot p_x^h = +0.02$, but the most significant contribution is at $V_0 \cdot p_x^h = -0.32$, where there is a global minimum in the imaginary part.

Although the assumption that the saddle point of $T(\mathbf{r}; \mathbf{p}^m, \mathbf{p}^h)$ occurs at real $\mathbf{p}^h$ is not true in general, numerical experimentation shows that this assumption is a sensible
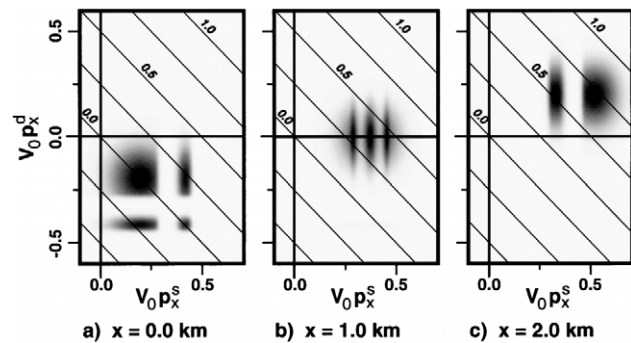

FIG. 3. The magnitude of the integrand of Equation (19) as a function of p_x^d and p_x^s, evaluated at the subsurface points (a) $(x, z) = (0, 5\ \text{km})$, (b) $(x, z) = (1\ \text{km}, 5\ \text{km})$, and (c) $(x, z) = (2\ \text{km}, 5\ \text{km})$. The diagonal lines are along loci of constant p_x^m.

means of finding a point near the actual saddle point. Exactly at the saddle point, a maximum in the real part of $T(\mathbf{r}; \mathbf{p}^m, \mathbf{p}^h)$ will coincide with the minimum in the imaginary part. Figure 4 shows that condition is close to being true for this example. Although not observable in Figure 4, the minimum and maximum of the real and imaginary parts of the traveltime can occur at slightly different values of real $\mathbf{p}^h$; the difference in the value of $T(\mathbf{r}; \mathbf{p}^m, \mathbf{p}^h)$ at these two locations, however, is negligible.

In Figure 3a, the major peak is at $V_0 \cdot p_x^s = 0.2$, $V_0 \cdot p_x^d = -0.2$. Rays that travel to the subsurface point unaffected by the low-velocity zone cause this peak. The contribution to the image from this peak occurs when equation (19) is evaluated along the path $V_0 \cdot p_x^m = 0.0$. Figure 4a shows the real and imaginary parts of the traveltime along this path. According to the proposed method, equation (19) will be approximated by equation (22) with T_0 equal to the value at which the imaginary part is a minimum. This evaluation misses the contributions from the smaller peak occurring at $V_0 \cdot p_x^s = 0.4$, $V_0 \cdot p_x^d = -0.4$, which is caused by the correlation between the late-arriving beams from both the shot and detector. Image contributions caused by correlation between the first-arrival from the shot beam and the later arrival from the detector beam and vice-versa are included by the evaluation along the paths at $V_0 \cdot p_x^m = \pm 0.2$.

Figure 3b shows three closely spaced peaks. These three contributions are caused by the triplication in the traveltimes. Since each of these three arrivals will be the single retained arrival at some value of p_x^m, each of the three arrivals will be represented in the image. Assuming that each of the complicated curves in Figures 4c and 4d results in contributions from a single-arrival, however, incorrectly describes the interference of the three events.

COMPUTATIONS

Working in the time domain is more efficient than computing in the frequency domain as prescribed by equations (9) and (18). Equation (9), for example can be rewritten as

$$I_0(\mathbf{r}) = -C_0 \sum_{\mathbf{L}} \iint dp_x' dp_y' \, \mathrm{Re}\big\{ A^*(\mathbf{r})$$
$$\times \bar{D}_{\mathbf{h}}[\mathbf{L}, \mathbf{p}', T^*(\mathbf{r})]_{\mathbf{h}=0}\big\}, \qquad (23)$$

where

$$\bar{D}_{\mathbf{h}} = D_{\mathbf{h}} + iH[D_{\mathbf{h}}], \qquad (24)$$

H denoting the Hilbert transform (see Aki and Richards, 1980, p. 157). Functions $A(\mathbf{r})$ and $T(\mathbf{r})$ are the complex amplitude and phase of the Gaussian beam u_{GB}. Since $T(\mathbf{r})$ is complex, $D_{\mathbf{h}}$ must be evaluated for complex arguments. This evaluation is done by transforming $D_{\mathbf{h}}$ from the Fourier domain to the time domain for complex sample values of time. Only a coarse sampling over a limited range of the imaginary time is necessary (Hill, 1990).

Evaluation of the beam paraxial traveltimes and ray amplitude for all image samples $\mathbf{r}$ would be computationally demanding. Because these traveltimes and amplitudes are smooth on the scale of a seismic wavelength, however, they can be computed on a coarse grid and interpolated to the finely sampled image grid (Hill, 1990; Thierry et al., 1999). A recursive algorithm (Hale, 1992a) is effective for evaluting beam traveltimes and amplitudes on a regular Cartesian grid.

For the prestack case, the coarse grid is also important for reducing the cost of evaluating summation (19). Reducing summation (19) to the approximation (22) requires sorting the
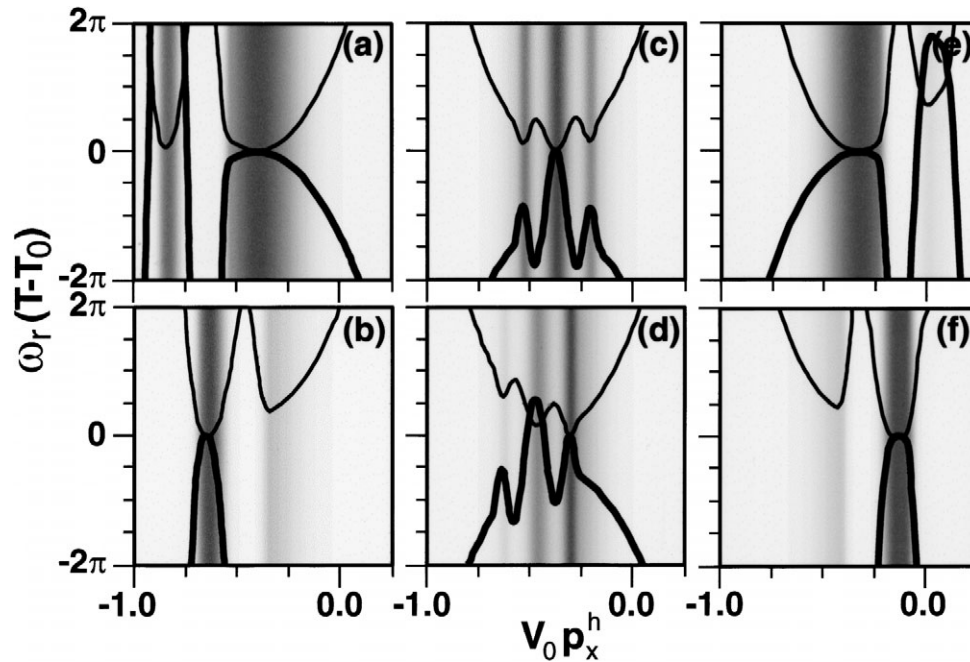

FIG. 4. The real (bold line) and imaginary (thin line) parts of $T(\mathbf{r}; \mathbf{p}^m, \mathbf{p}^h)$ along constant p_x^m paths through peak amplitudes appearing in Figure 3: (a) $x = 0$ m, $V_0 p_x^m = 0$, $T_0 = (4.079 \text{ s}, 0.000 \text{ s})$; (b) $x = 0$ m, $V_0 p_x^m = 0.2$, $T_0 = (4.1524 \text{ s}, 0.001 \text{ s})$; (c) $x = 1000$ m, $V_0 p_x^m = 0.38$, $T_0 = (4.182 \text{ s}, 0.000 \text{ s})$; (d) $x = 1000$ m, $V_0 p_x^m = 0.28$, $T_0 = (4.164 \text{ s}, 0.000 \text{ s})$; (e) $x = 2000$ m, $V_0 p_x^m = 0.72$, $T_0 = (4.372 \text{ s}, 0.000 \text{ s})$; (f) $x = 2000$ m, $V_0 p_x^m = 0.53$, $T_0 = (4.431 \text{ s}, 0.000 \text{ s})$. The time axes are scaled by a reference frequency $\omega_r = 2\pi \cdot 20$ Hz. The gray-scale density is proportional to the magnitude of the integrand of equation (19).

travel times. The traveltimes are most efficiently generated for each beam at all positions **r** near each raypath as the rays are shot as a function of initial ray directions $\mathbf{p}^s$ and $\mathbf{p}^d$. On the other hand, the summation (19) must access these traveltimes at each location **r** as a function of $\mathbf{p}^h$ and then $\mathbf{p}^m$. This sorting is more efficient on a coarse grid because there are fewer samples and all these samples will fit into computer memory at once.

Gaussian beam migration requires the choice of an initial beam width. As reported in an earlier article (Hill, 1990), the results are not sensitive to this choice as long as the initial width is near the value

$$w_\ell = \frac{2\pi V_a}{\omega_\ell}, \tag{25}$$

where V_a is a global spatial average of the velocities occurring in the velocity model and the reference frequency ω_ℓ is at the lower end of the seismic data bandwidth.

The spacing of the beams, both in initial spatial position and initial direction, depends on the frequency content of the data. The constant a in partition function (6) governs the spatial sampling. Approximation (6) is a convolution of a two-dimensional Gaussian function of width $w_\ell\sqrt{\omega_\ell/\omega}$ with a two-dimensional lattice of Dirac delta functions. The delta functions are separated by distance a. Therefore, the two-dimensional spatial Fourier transform of the left side of equation (6) becomes a product of a Gaussian function of width $w_\ell^{-1}\sqrt{\omega/\omega_\ell}$ with a lattice of Dirac delta functions spaced by a distance $2\pi/a$. This product will be approximately equal to the single delta located at the center of the transformed Gaussian function if the spacing of the delta functions in this transformed lattice is large compared to the width of transformed Gaussian function. Therefore, if the constant a is small enough, this product will approximately equal the transform of the right-hand side of equation (6), which is a single delta function at the origin. Numerical experimentation demonstrates that for a hexagonal lattice, a good value for the nearest-neighbor spacing a is

$$a = 2w_\ell\sqrt{\frac{\omega_\ell}{\omega_h}}, \tag{26}$$

where ω_h represents the higher end of the data bandwidth.

The sampling in initial direction must be sufficiently small so that the beams superimposed to form the Green's function will form a band-limited, unaliased point wavefield at the source location. This condition implies that for points near the source, the traveltime must change by less than one-half period from one beam to the next. Since the initial beam width at frequency ω is $w = w_\ell\sqrt{\omega_\ell/\omega}$, the change in traveltime at a distance of $2w$ from the beam origin is $2w \cdot \Delta p$ when the initial direction changes by Δp. In order for the change in traveltime to be less than one-half period, the sampling must be about

$$\Delta p_x = \Delta p_y = \frac{1}{w_\ell\sqrt{\omega_\ell\omega_h}}. \tag{27}$$

These sampling choices are similar to the one reported earlier (Hill, 1990), although slightly revised for the three-dimensional case. These sampling intervals are only rules of thumb expressed by the latitude in the choice of ω_ℓ and ω_h. These values depend on the data set but are typically about 60 and 300 rad/s (10 and 50 Hz).

RESULTS

The Marmousi synthetic data (Versteeg and Grau, 1990; Versteeg, 1994) tests an imaging method's ability to handle multivalued traveltimes. The Marmousi model contains strong lateral velocity variations that cause complicated multipathing of the seismic energy (Geoltrain and Brac, 1993). This multipathing precludes the use of simple first-arrival traveltimes, although good images are obtained using most-energetic-arrival methods (Geoltrain and Brac, 1993; Gray and May, 1994; Nichols, 1996; Audebert et al., 1997). This section presents some results of applying prestack Gaussian beam migration to this data set.

The following Gaussian beam migrations of the Marmousi data use a layered representation of the velocity model (Figure 5). Layer boundaries within the model represent all the large velocity discontinuities; smaller velocity variations within layers are represented on grids. The layer boundaries are not smoothed and have corners where necessary to represent the shape of large velocity discontinuities. The gridded velocities within layers are smoothed with a 60-m bell-shaped window.

Figure 6 shows the impulse response of poststack Gaussian beam migration for the Marmousi velocity model and compares it to the response from a full-waveform 45° finite-difference method (Claerbout, 1985). The velocity model used for the finite-difference migration was slightly smoothed to suppress lateral reflection of energy from layer boundaries. The comparison shows that even with the large velocity variations, the Gaussion beam method retains most of the prominent features of the impulse response compared to the finite-difference method. The largest differences are in the diffracted portions of the response.

In addition to the approximations inherent in the beams, the proposed method of prestack migration involves the approximations described for evaluating summation (19). Figure 7b shows the impulse response of prestack Gaussian beam to an impulse on a common-offset section. Figure 7a shows the full-wavefield response generated by a 45° finite-difference shot-profile migration for shot and detector impulse positions that are the same as for the common-offset data. The two responses are comparable, although the details differ, especially in the diffracted wavefield.
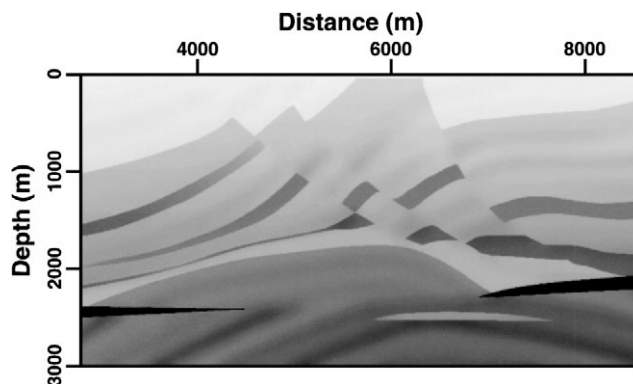

FIG. 5. The Marmousi velocity model used by the Gaussian beam depth migration. Layer boundaries represent major velocity discontinuities. Velocity variations within layers are smoothed.

Figure 8 shows the image formed by prestack Gaussian beam migration of the Marmousi data set. The method has formed an image of the anticline at $(x, z) = (6200$ m, 2500 m), where the energy is strongly affected by the complex velocity variations. The structure of the image is correct. The reflection amplitudes waver, however, probably because rapidly varying illumination levels are not properly handled by the current method, which only emphasizes the imaging kinematics. Images of Marmousi produced by other methods appear in Geoltrain and Brac (1993), Gray and May (1994), Nichols (1996), Audebert et al.

(1997), Operto et al. (1998), Han (1998), Huang et al. (1999), and Thierry et al. (1999).

DISCUSSION AND CONCLUSIONS

The first approximation introduced by the proposed method of migration is the Gaussian beam itself. If there are significant velocity variations on the scale of a beam width, the paraxial approximation will be accurate near the raypath but will not be a good description of the wavefronts across the width of the beam. Nevertheless, even when strong velocity variations cause individual beams to be inaccurate away from the raypath, the migration usually produces a good image because many beams are summed to form the image and all of these beams are accurate where their amplitudes are largest, near the central ray. For example, Figure 9 shows images of the Marmousi data set produced for two choices of initial beam width, which are both near the suggested value (25). Because of the different initial width and the conditions on beam sampling (26) and (27), the two migrated images are sums of completely different sets of beams. These beams encounter abrupt velocity changes
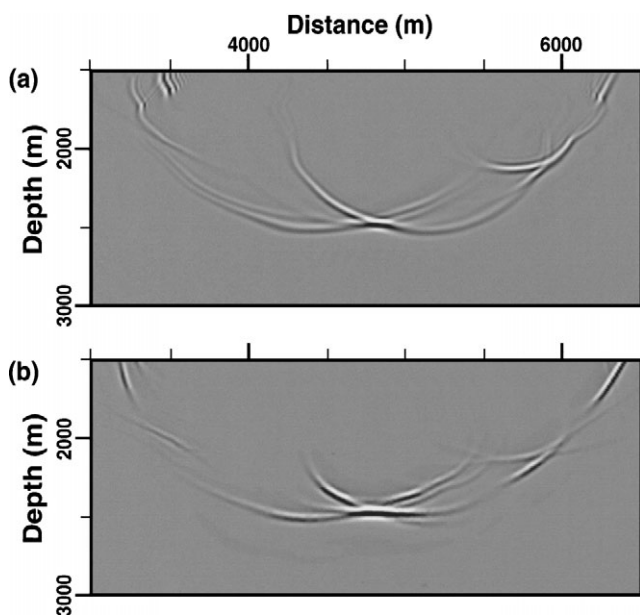

FIG. 6. The response of poststack (a) 45° finite-difference migration and (b) Gaussian beam migration to an impulse at $x = 5200$ m, $t = 2.0$ s.

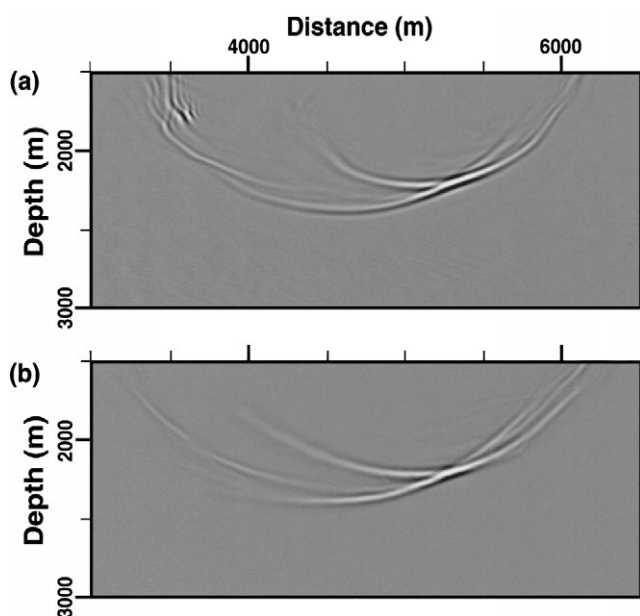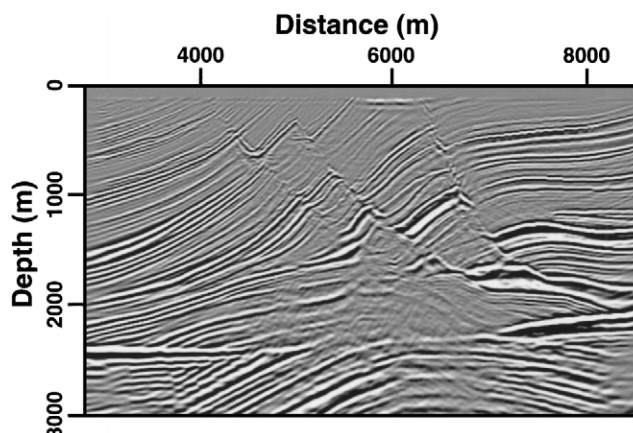FIG. 8. The Marmousi image computed by prestack Gaussian beam migration for the initial beam width $w_\ell = 200$ m.

FIG. 7. The response of prestack (a) 45° finite-difference migration and (b) Gaussian beam migration to an impulse at source position $x_s = 4000$ m, detector position $x_d = 5200$, $t = 2.0$ s.
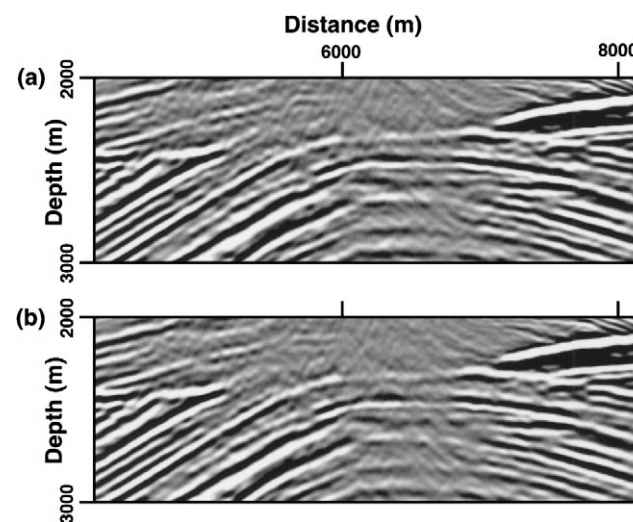

FIG. 9. A comparison of image computed by prestack Gaussian beam migration for the initial beam widths (a) $w_\ell = 200$ m and (b) $w_\ell = 150$ m.

across steeply dipping interfaces. Although some beams cannot be accurate across their entire width, the sum of the beams produces a good image, which is stable with respect to choice of the initial width.

A second important approximation introduced by the present method is the evaluation of the summation (19). The method described here has the virtues of being simple and quick to evaluate. Figures 3 and 4 illustrate that this method will retain most multipath arrivals but can miss some and can improperly describe the interference between arrivals. Moreover, the computed amplitudes are not accurate. These shortcomings could be addressed by more elaborate methods of evaluating (19). For example, the amplitudes could be computed by using the dynamic ray-tracing information to expand the traveltimes about the saddle point and doing a steepest-descents evaluation. Another improvement would be extending approximation (22) to include several closely spaced arrivals.

Although the Gaussian beam method is complicated, it can be efficient. One reason is that the traveltime field for each beam must be a simple, smooth function and, therefore, can be computed on a relatively coarse grid and interpolated to the finer sampling required for the image. Although the complicated computations for obtaining the values of traveltime and amplitude at each coarse-grid point are costly, these values are used many times to sum the beam into the many image points on the fine grid contained within the cell. This coarse-grid technique is especially important for the computation of three-dimensional output because each cell of the coarse grid will contain several hundred image-grid points. Another reason Gaussian beam migration can be efficient is that it replaces the standard Kirchhoff operation of summing each trace into a large three-dimensional volume by the summation of each beam into a volume confined about the raypath (Hale, 1992a, b; Sun and Schuster, 1999).

Prestack Gaussian beam migration retains Kirchhoff migration's flexibility for restricting the migrated output image to targeted subvolumes or planes. Because it requires common-offset, common-azimuth input, however, the Gaussian beam method presented in this paper is less flexible than the Kirchhoff method for accepting input data acquired with irregular source-detector spacings. Preparing common-offset input for this Gaussian beam migration method often requires regularization of the data offset sampling.

Perhaps when computers are fast enough, there will be no need for anything but full waveform imaging. These methods will completely handle multipath effects. On the other hand, with this speed, there will also be new roles for high-frequency methods such as Gaussian beams. One frequently mentioned advantage is that raypath methods are an interpretation of the wavefield, separating it into conceptual components, such as *P*-wave and *S*-wave. Regardless of computer speed, this conceptualization of the wavefield will always have a role in the analysis and interpretation of seismic energy.

ACKNOWLEDGMENTS

REFERENCES

Aki, K., and Richards, P. G., 1980, Quantitative seismology: W. H. Freeman.

Audebert, F., Nichols, D., Rekdal, T., Biondo, B., Lumley, D. E., and Urdaneta, H., 1997, Imaging complex geologic structure with single-arrival Kirchhoff prestack depth migration: Geophysics, **62**, 1533–1543.

Bleistein, N., 1999, Hagedoorn told us how to do Kirchhoff migration and inversion: The Leading Edge, **18**, 918–927.

Cerveny, V., 1985, The application of ray tracing to the propagation of shear waves in complex media, *in* Dohr, G. P., Ed., Handbook of geophysical exploration: Seismic shear waves: Geophysical Press 1–124.

Claerbout, J. F., 1970, Coarse grid calculations of waves in inhomogeneous media with applications to delineation of complicated seismic structure: Geophysics, **35**, 407–418.

——— 1976, Fundamentals of geophysical data processing: McGraw-Hill.

——— 1985, Imaging the earth's interior: Blackwell Scientific Publ.

Geoltrain, S., and Brac, J., 1993, Can we image complex structures with first-arrival traveltimes?: Geophysics, **58**, 564–575.

Gray, S. H., and May, W. P., 1994, Kirchhoff migration using eikonal equation traveltimes: Geophysics, **59**, 810–817.

Hale, D., 1992a, Computational aspects of Gaussian beam migration: Colorado School of Mines Center for Wave Phenomena Report 139.

——— 1992b, Migration by the Kirchhoff, slant stack, and Gaussian beam methods: Colorado School of Mines Center for Wave Phenomena Report 121.

Han, B., 1998, A comparison of four depth-migration methods: 68th Ann. Internat. Mtg., Soc. Expl. Geophys., Expanded Abstracts, 1104–1107.

Huang, L., Fehler, M. C., Roberts, P. M., and Burch, C. C., 1999, Extended local Rytov Fourier migration method: Geophysics, **64**, 1535–1545.

Hill, N. R., 1990, Gaussian beam migration: Geophysics, **55**, 1416–1428.

Nichols, D. E., 1996, Maximum energy traveltimes calculated in the seismic frequency band: Geophysics, **61**, 253–263.

Operto, S., Xu, S., Lambare, G., 1998, Can we image quantitatively complex models with rays?: 68th Ann. Internat. Mtg., Soc. Expl. Geophys., Expanded Abstracts, 1120–1123.

Schneider, W., 1978, Integral formulation for migration in two and three dimensions: Geophysics, **43**, 49–76.

Sun, H., and Schuster, G. T., 1999, Wavepath migration versus Kirchhoff migration: 69th Ann. Internat. Mtg., Soc. Expl. Geophys., Expanded Abstracts, 1138–1141.

Thierry, P. Operto, S., and Lambare, G., 1999, Fast 2-D ray+Born migration/inversion in complex media: Geophysics, **64**, 162–181.

Versteeg, R. 1994, The Marmousi experience: Velocity model determination on a synthetic complex data set, The Leading Edge, **13**, 927–936.

Versteeg, R., and Grau, G., 1990, Practical aspects of seismic data inversion, the Marmousi experience, Eur. Assoc. Expl. Geophys. Proc. 1990 EAEG Workshop, 52nd EAEG Mtg., 1–194.

APPENDIX A

GAUSSIAN BEAMS

This appendix summarizes three-dimensional Gaussian beams and presents a simple beam parameterization that is used for the migration method reported in this paper. A full description of Gaussian beams in the context of dynamic ray theory appears in a review by Cerveny (1985).

In the neighborhood of a raypath, the expansion of the traveltime field to second order in ray-centered coordinates is

$$T(q_1, q_2, s) \approx \tau(s) + \frac{1}{2}\mathbf{q}^T\mathbf{M}(s)\mathbf{q}, \qquad \text{(A-1)}$$

where s is arc length along the ray, and q_1 and q_2 are coordinates along the axes $\hat{e}_1$ and $\hat{e}_2$ that lie in a plane perpendicular to the ray at point s (see Cerveny, 1985). The axes $\hat{e}_1$ and $\hat{e}_2$ are constructed such that the coordinates (q_1, q_2, s) form a right-handed, orthogonal, curvilinear system. Function $\tau(s)$ is travel time along the raypath

$$\tau(s) = T(0, 0, s). \qquad \text{(A-2)}$$

Vector $\mathbf{q}$ is a two-dimensional vector,

$$\mathbf{q}^T = (q_1, q_2). \qquad \text{(A-3)}$$

The elements of the 2×2 matrix $\mathbf{M}(s)$ are the second derivative of the traveltime field with respect to the coordinates q_1 and q_2:

$$M_{IJ}(s) = \left[\frac{\partial^2 T(q_1, q_2, s)}{\partial q_I \partial q_J} \right]_{q_1=q_2=0}. \qquad \text{(A-4)}$$

Expansion (A-1) contains no first-order derivatives because, for the isotropic case considered in this paper, constant traveltime surfaces are perpendicular to rays.

A way to determine the matrix $\mathbf{M}(s)$ is to substitute equation (A-1) into the eikonal equation written in ray-centered coordinates. This step yields a nonlinear, ordinary differential equation for $\mathbf{M}(s)$. The standard procedure of dynamic ray tracing is to reduce this equation to the linear system

$$\frac{d\mathbf{Q}(s)}{ds} = v(s)\mathbf{P}(s) \qquad \text{(A-5)}$$

$$\frac{d\mathbf{P}(s)}{ds} = v^{-2}(s)\mathbf{V}(s)\mathbf{Q}(s), \qquad \text{(A-6)}$$

where $\mathbf{P}(s)$ and $\mathbf{Q}(s)$ are 2×2 matrices such that

$$\mathbf{M}(s) = \mathbf{P}(s)\mathbf{Q}^{-1}(s). \qquad \text{(A-7)}$$

Matrix $\mathbf{V}(s)$ is a 2×2 matrix of second derivative of the velocity field

$$V_{IJ} = \frac{\partial^2 v}{\partial q_I \partial q_J}. \qquad \text{(A-8)}$$

Since the traveltime field (A-1) satisfies the eikonal equation in the vicinity of the raypath, the transport equation can then be invoked to determine the amplitudes of a high-frequency solution to the scalar wave equation (1). The resulting solution is

$$\sqrt{\frac{v(s) \det \mathbf{Q}(s_0)}{v(s_0) \det \mathbf{Q}(s)}} \exp\left\{ i\omega\left[\tau(s) + \frac{1}{2}\mathbf{q}^T\mathbf{M}(s)\mathbf{q} \right] \right\}, \quad \text{(A-9)}$$

normalized to unity at $s = s_0$.

The character of solution (A-9) is determined by the initial conditions chosen for matrix functions $\mathbf{P}$ and $\mathbf{Q}$. For any choice of real $\mathbf{P}$ and $\mathbf{Q}$, there might be points along the raypath where solution (A-9) fails because $\det \mathbf{Q} = 0$. On the other hand, complex initial values of $\mathbf{P}$ and $\mathbf{Q}$ can be chosen so that (A-9) is always a bounded, high-frequency solution of the scalar wave equation. If the choice of complex initial values is such that $\text{Im}\{\mathbf{P}\mathbf{Q}^{-1}\}$ is positive definite and $\det \mathbf{Q} \neq 0$, then these qualities hold everywhere along the raypath. In this case, equation (A–9) is the well-known Gaussian-beam asymptotic solution to the wave equation (Cerveny, 1985). The particular initial-value choice

$$\mathbf{P}_0 = \begin{pmatrix} i/V_0 & 0 \\ 0 & i/V_0 \end{pmatrix} \qquad \text{(A-10)}$$

$$\mathbf{Q}_0 = \begin{pmatrix} \omega_\ell w_\ell^2/V_0 & 0 \\ 0 & \omega_\ell w_\ell^2/V_0 \end{pmatrix} \qquad \text{(A-11)}$$

results in a beam with initial width w_ℓ at frequency ω_ℓ. Quantity V_0 is the seismic velocity at the ray's initial point s_0.

APPENDIX B

REPRESENTATION OF A POINT SOURCE BY GAUSSIAN BEAM SUMMATION

The field from a point source at $\mathbf{r}'$ is approximated by the Gaussian beam summation

$$G(\mathbf{r}, \mathbf{r}'; \omega) = \int d\Omega \Psi(\Omega) u_{GB}(\mathbf{r}; \mathbf{r}', \Omega; \omega), \qquad \text{(B-1)}$$

where function u_{GB} is the value at point $\mathbf{r}$ of a Gaussian beam that departs from point $\mathbf{r}'$ at angle $\Omega = (\theta, \phi)$, and $d\Omega$ is the solid angle $\sin\theta \cdot d\theta\, d\phi$. The spherical coordinates are such that point $\mathbf{r}'$ is at the origin and point $\mathbf{r}$ is on the axis $\theta = 0$. Function $\Psi(\Omega)$ must be determined. If the velocity field is constant $v(\mathbf{r}) = V_0$, then by symmetry, this function is constant, $\Psi(\Omega) = \Psi_0$. This constant Ψ_0 will also be appropriate if the

actual medium is nearly constant for a few wavelengths about the source, but is more complicated elsewhere.

In a constant velocity medium, the Gaussian beam given by equations (A-9)–(A-11) simplifies to

$$u_{GB} = \frac{\omega_\ell w_\ell^2}{V_0}\left(\frac{\omega_\ell w_\ell^2}{V_0} + is \right)^{-1}$$

$$\times \exp\left\{ i\omega\left[\frac{s}{V_0} + \frac{i}{2}\frac{q_1^2 + q_2^2}{\omega_\ell w_\ell^2 + i V_0 s} \right] \right\}. \qquad \text{(B-2)}$$

Then equation (B-1) becomes

$$G = \Psi_0 \int_0^{2\pi} d\phi \int_0^{\pi} \sin\theta \cdot d\theta \frac{\omega_\ell w_\ell^2}{\omega_\ell w_\ell^2 + i V_0 R \cos\theta}$$

$$\times \exp\left\{ i\omega \left[\frac{R\cos\theta}{V_0} + \frac{i}{2} \frac{R^2 \sin^2\theta}{\omega_\ell w_\ell^2 + i V_0 R \cos\theta} \right] \right\} \quad \text{(B-3)}$$

where $R = |\mathbf{r} - \mathbf{r}'|$. A stationary point of the integral occurs at $\theta = 0$. Since for large ω, the principal contribution to the integral occur near this stationary point, equation (B-3) can be approximated as

$$G = 2\pi \Psi_0 \left(\frac{\omega_\ell w_\ell^2}{\omega_\ell w_\ell^2 + i V_0 R} \right) \exp(i\omega R / V_0)$$

$$\cdot \int_0^{\infty} \theta \exp\left\{ \frac{-i\omega}{2} \frac{R}{V_0} \left[\frac{\omega_\ell w_\ell^2}{\omega_\ell w_\ell^2 + i V_0 R} \right] \theta^2 \right\} d\theta \quad \text{(B-4)}$$

Evaluation of the definite integral results in

$$G = \Psi_0 \left(\frac{-2\pi i V_0}{\omega} \right) \frac{\exp(i\omega R / V_0)}{R}. \quad \text{(B-5)}$$

Equation (B-6) is the well-known response for a constant velocity if

$$\Psi_0 = \frac{i\omega}{2\pi V_0}. \quad \text{(B-6)}$$

For the derivation in this paper, it is more convenient to change integration variables from θ and ϕ to ray-parameters p_x' and p_y':

$$p_x' = \frac{1}{V_0} \sin\theta \cos\phi$$

$$p_y' = \frac{1}{V_0} \sin\theta \sin\phi \quad \text{(B-7)}$$

$$p_z' = \frac{1}{V_0} \cos\theta.$$

With these variable changes and equation (B-6), the Green's function (B-1) becomes

$$G(\mathbf{r}, \mathbf{r}'; \omega) = \frac{i\omega}{2\pi} \int \frac{dp_x' dp_y'}{p_z'} u_{GB}(\mathbf{r}; \mathbf{r}', \mathbf{p}'; \omega). \quad \text{(B-8)}$$